

Digital Volume Correlation: Three-dimensional Strain Mapping Using X-ray Tomography

by B. K. Bay, T. S. Smith, D. P. Fyhrie and M. Saad

ABSTRACT—A three-dimensional extension of two-dimensional digital image correlation has been developed. The technique uses digital image volumes generated through high-resolution X-ray tomography of samples with microarchitectural detail, such as the trabecular bone tissue found within the skeleton. Image texture within the material is used for displacement field measurement by subvolume tracking. Strain fields are calculated from the displacement fields by gradient estimation techniques. Estimates of measurement precision were developed through correlation of repeat unloaded data sets for a simple sum-of-squares displacement-only correlation formulation. Displacement vector component errors were normally distributed, with a standard deviation of 0.035 voxels (1.22 μm). Strain tensor component errors were also normally distributed, with a standard deviation of approximately 0.0003. The method was applied to two samples taken from the thigh bone near the knee. Strains were effectively measured in both the elastic and postyield regimes of material behavior, and the spatial patterns showed clear relationships to the sample microarchitectures.

KEY WORDS—Strain measurement, X-ray tomography, image correlation, trabecular bone

Many advanced synthetic foams and composites, and virtually all naturally occurring materials, present tremendous challenges to both the experimental and analytical branches of mechanics. Analytical methods must account for anisotropy, inhomogeneity and even nonlinearity in the elastic range, complex yield criteria and postyield behavior that can include hardening, softening, collapse and rebound phenomena. Determination of the extensive sets of constitutive parameters required for these materials, and validation of analytical results, is often beyond the capabilities of standard experimental techniques.

The same features that generate complex behavior within these materials, however, also provide the opportunity for a new type of experimental strain mapping. Mixtures of different component materials, hierarchical microarchitectures and large-scale inclusions and voids are the tools used by

both nature and the engineer to tune material behavior over a broad range of loading conditions. These same features are, in many instances, imageable in three dimensions by modern tomographic techniques. For materials of this type, we have developed a technique for estimating the full continuum-level strain tensor in three dimensions throughout the interior of test samples by correlating imaging volumes of the samples in unloaded and loaded states.

The new method, *digital volume correlation*, is an extension of standard digital image correlation,^{1–5} a technique that has found numerous applications^{6–8} and has been extensively characterized.^{9–11} Digital volume correlation relies on the X-ray tomographic imaging of naturally occurring material texture within samples. X-ray-based approaches have been used in two dimensions for both applied radio-opaque surface speckle¹² and naturally occurring material microarchitecture.¹³ Digital volume correlation is a true three-dimensional technique that estimates internal sample strains from displacement measurements, and is distinct from the three-dimensional surface deformation techniques that rely on two-angle planar images.^{14,15}

High-resolution X-ray tomography has been used by numerous laboratories to investigate trabecular bone microarchitecture.^{16–20} There have also been applications in more traditional engineering and physical science settings. It has been used as a nondestructive inspection tool for the visualization of internal flaws and damage^{21–25} and for the identification of internal material inhomogeneities.^{26–29} Functional evaluations have included the measurement of permeability within geological samples^{30,31} and the visualization of internal cracks within samples under load.³² Digital volume correlation adds the evaluation of full-field mechanical response to the applications of X-ray tomography.

This paper presents a description of digital volume correlation, an assessment of measurement precision and an example application. The material studied is trabecular bone, a high-porosity rigid foam that is a key structural material in the human skeleton. Characterizing the mechanics of trabecular bone is critical to many problems in the biomedical engineering of replacement materials and components used by orthopaedic surgeons in the treatment of skeletal trauma and pathology. In addition to its medical importance, trabecular bone is as constitutively complex as any synthetic material and, thus, is a useful material for the development of advanced strain measurement techniques. The methods described here are immediately applicable to other structural foams, and with slight tuning will likely be successful for a much broader range of materials.

B. K. Bay is Assistant Professor, and T. S. Smith is Research Assistant, Orthopaedic Research Laboratories, Department of Orthopaedic Surgery, University of California, Davis, Sacramento, CA 95817. D. P. Fyhrie is Head of the Biomechanics Section, and M. Saad is Technician, Breech Research Laboratory, Bone and Joint Center, Henry Ford Hospital, Detroit, MI 48202.

Original manuscript submitted: May 1, 1998.
Final manuscript received: January 22, 1999.

Method

Three-dimensional digital volume correlation involves three main steps: (1) generation of volume images of samples in unloaded and loaded states, (2) measurement of a discrete displacement vector field throughout the sample by a correlation procedure, and (3) calculation of the strain tensor field from the displacement vector field. Each of these steps is described in detail below. Afterward, experiments for the characterization of measurement precision are detailed.

Generation of Volume Images

Digital volume correlation employs volumes of image data that are analogous to the planar images used for standard two-dimensional correlation procedures. High-resolution X-ray tomography is used to generate the volume images, although any type of tomography could potentially be used if it has adequate geometric fidelity and reasonable noise characteristics.

The scanner used for these experiments was the microCT system in the Bone and Joint Research Center at Henry Ford Hospital in Detroit, Michigan.³³ The system is a flexible geometric magnification design that can accommodate samples from 3 to 50 mm in diameter. The samples used in this study were cylinders of trabecular bone 15 mm in diameter and 18 mm high, bonded with cyanoacrylate to flat surface acrylic platens. They were positioned for axial compression within a stepper-motor-controlled loading system that contained an X-ray transparent polycarbonate standoff tube (Fig. 1). Scanning was conducted at 50 kVp and 0.2 mA with a 20- μ m focal spot tungsten anode. Area projections were gathered with an image intensifier/CCD detector for 400 angles distributed evenly through 360 deg of sample rotation. Total scan time was approximately 40 min.

Reconstruction of the image volumes, which depict the detailed internal microarchitecture of the entire sample, was accomplished with a cone beam algorithm.³⁴ Data sets produced by the reconstruction procedure contained 580 cross-sectional images of 520×520 voxels. Each voxel was a 35- μ m cube with a gray-scale depth of 16 bit (65,536 possible intensity values). Examination of representative cross sections revealed that the bone tissue fell between voxel intensity values of 100 and 700. To reduce the size of the image data sets and eliminate the influence of background noise on the volume correlation procedure, new image data sets of 8-bit depth (256 possible intensity values) were produced by linearly mapping values between 100 and 700 to the range 1 to 255. Voxels outside of this range were assigned a value of zero. Each data volume after scaling to 8 bit occupied approximately 150 Mb of computer storage.

General Description of Digital Volume Correlation

The core of the technique is the measurement of a discrete displacement vector field by correlation of image volumes of the sample under load with image volumes of the unloaded sample. The method is analogous to the measurement of surface strains by digital image correlation in materials with natural variations in image intensity. Variations in voxel intensity within the image volumes form the basis of the correlation pattern matching. Subvolumes around a given point where a displacement value is sought are located in three dimensions within the loaded data set.

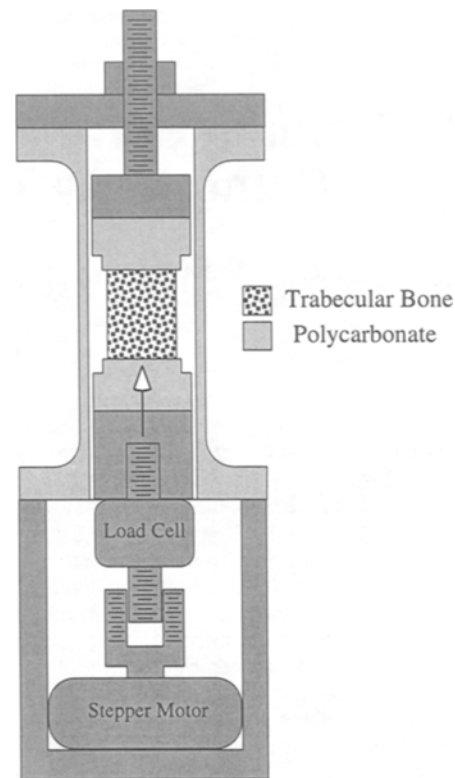


Fig. 1—The apparatus used for microCT scanning of trabecular bone samples under load

The algorithm for displacement measurement (Fig. 2) represents the need to satisfy three competing requirements. Similar to two-dimensional correlation, displacement measurement must be accurate to much better than the voxel level to resolve elastic range strains. Subvoxel minimization embodying cubic order interpolation of the volume image data is used to achieve this accuracy. Accuracy competes with the need for fast measurement of displacement at any given point. For spatially refined measurements, the discrete displacement field must be dense; approximately 5500 points evenly distributed throughout the sample volume are used in a typical measurement. Finally, the nonlinear minimization required for each displacement measurement must be robust to prevent inaccurate displacement measurements from corrupting the strain calculation. Accuracy and speed are balanced by applying Gauss-Newton minimization to a sum-of-squares objective function, with the cubic order interpolation analytically incorporated into the objective function derivatives. Robust minimization is ensured by careful prediction of minimization starting points and monitoring of convergence characteristics.

The input to the three-dimensional texture correlation algorithm consists of the two 8-bit image volumes (undeformed and deformed) and a file that specifies the locations at which measurements are desired. For each measurement location, a subvolume centered around the measurement location is extracted from the undeformed image volume. The correlation problem can be described conceptually as finding the location within the deformed image data that best matches the undeformed subvolume.

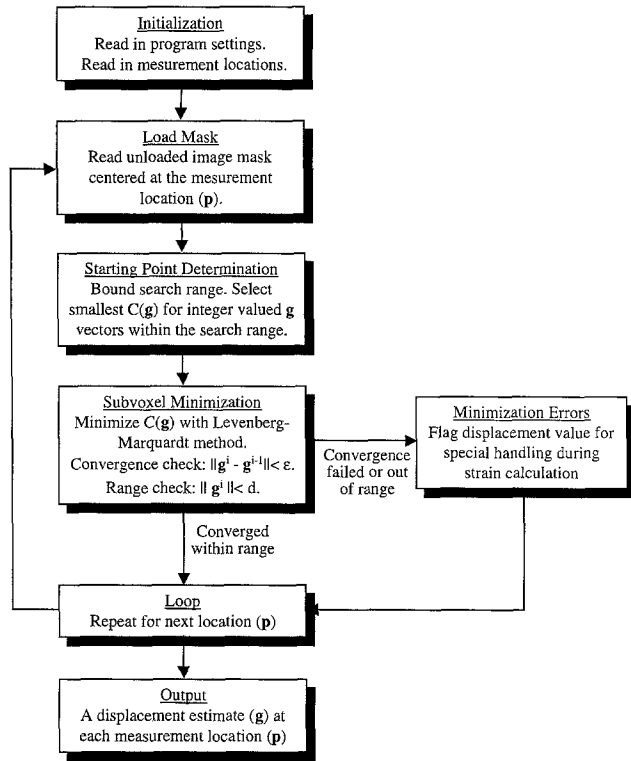


Fig. 2—Flowchart of the displacement measurement routine

Formal Problem Statement

The problem of locating subvolumes is formulated mathematically as an unconstrained minimization. An objective function is defined that quantifies the degree of match between subvolumes in the undeformed and deformed image data. Minimizing this function defines a displacement vector at a given point. We have defined the digital volume correlation problem as

$$\min_{\mathbf{g} \in \mathcal{R}^3} C(\mathbf{g}) = \frac{1}{2} \sum_{i=1}^w \{B(\mathbf{p} + \mathbf{g} + \mathbf{m}_i) - A(\mathbf{p} + \mathbf{m}_i)\}^2, \quad (1)$$

where $\mathbf{p} = p(s, r, c)$ is the displacement measurement location (center of an undeformed subvolume), $\mathbf{g} = g(s, r, c)$ is a trial displacement vector, $\mathbf{m}_i = m_i(s, r, c)$ is an offset to a location within a subvolume, w is the number of points within a subvolume, A are the values from the unloaded image data, B are the values from the loaded image data and s, r, c are the slice, row, column image coordinates, respectively. A subvolume is a region of image data centered on a given location. In three dimensions, this is a small cube of w image values. The objective function is evaluated by summing the squared differences between values in an undeformed subvolume (A) centered on location \mathbf{p} and values in a deformed subvolume (B) offset from this location by a vector \mathbf{g} . The vector \mathbf{p} is assigned integer values to align the undeformed subvolume with voxels of the unloaded image volume; \mathbf{g} , however, is treated as a real-valued vector. Locations within an image volume are specified in an orthogonal slice, row, column coordinate system.

This statement of the correlation problem is different than standard digital image correlation in two important respects,

both prompted by the added computational burdens of three-dimensional analysis. First, a displacement-only formulation has been implemented. Rigid body rotations and subvolume strains are not considered. These additional parameters can be incorporated within the same overall framework (at some additional computational expense). Second, correlation procedures traditionally use a cross-correlation objective function, but a simple sum-of-squares function has been used here. The advantage of a sum-of-squares function is that minimization can be accomplished efficiently with Gauss-Newton techniques. The disadvantage is a greater sensitivity to differences in overall background intensity levels between undeformed and deformed image data sets. This appears to be less of a problem, however, with images derived through tomography than with direct optical surface images.

Starting Point Determination

A fundamental step in all nonlinear minimizations is selection of an accurate starting point. It is essential to select a starting point in the vicinity of a global minimum and avoid local minima. With minimization techniques that employ derivative information, it is also important to be relatively close to the minimum for assumptions about the shape of the minimum to be valid. Two procedures are used to attempt to satisfy both conditions.

First, a search range of voxel locations within the deformed image data is identified. The center of the range is initially set to the voxel coordinates of the undeformed subvolume center (a null \mathbf{g} vector). As displacement measurements accumulate, however, this information is used to predict displacements for unknown points. A connectivity array is generated that contains the nearest neighbors of each measurement point. The average of all points within this array that have already been located is used as the starting point for measurement of displacement at new points. The size of the search range is set to the maximum displacement expected for any point within the sample.

Next, a coarse estimate of the minimum is determined by calculation of the objective function for every integer value of \mathbf{g} within the search range. The location determined during this direct minimization step becomes the starting point for formal subvoxel minimization, as described below. This point will lie within one voxel of the true minimum.

Minimization to Subvoxel Precision

We have used the Levenberg-Marquardt variation of the Gauss-Newton technique³⁵ for minimization to the subvoxel level. This approach is specifically designed to efficiently minimize objective functions that have a sum-of-squares form. Standard Newton minimization assumes minima of quadratic form and makes use of second derivative information (the Hessian matrix) for the prediction of search directions within parameter space. For objective functions of sum-of-squares form, the Hessian can be approximated from first-derivative information, which is much simpler to estimate. The general minimization technique is described by

$$\min_{\mathbf{x} \in \mathcal{R}^n} \frac{1}{2} \sum_{i=1}^w f_i(\mathbf{x})^2 \quad (2)$$

$$(J_k^T J_k + \lambda_k I) p_k = -J_k^T f_k, \quad (3)$$

where J_k is the Jacobian matrix of $f_i(x)$, λ_k is a nonnegative constant and p_k is the correction term for the next iteration ($x_{k+1} = x_k + p_k$). For the specific objective function form used here [eq (1)], the terms required for calculation of the correction vector become

$$f_i(\mathbf{g}) = B(\mathbf{p} + \mathbf{g} + \mathbf{m}_i) - A(\mathbf{p} + \mathbf{m}_i) \quad (4)$$

$$J_{i,j} = \frac{\partial}{\partial g_j} f_i(\mathbf{g}) = \frac{\partial}{\partial g_j} \{B(\mathbf{p} + \mathbf{g} + \mathbf{m}_i) - A(\mathbf{p} + \mathbf{m}_i)\}. \quad (5)$$

The method requires both objective function values and the Jacobian of the objective function at arbitrary real-valued locations within the deformed subvolumes. Since image data exist only at integer voxel locations, interpolation is used to estimate data at intermediate locations.

Interpolation of the Image Data

We have used a tricubic interpolation scheme based on products of one-dimensional Hermitian cardinal basis functions.³⁶ The domain over which interpolation occurs is a unit cube, with each vertex of the cube a voxel of the image data. Interpolation involves calculating values between voxels from nodal values taken from the image data and basis functions defined continuously within the unit cube.

The four one-dimensional Hermitian cardinal basis functions and their derivatives are

$$\begin{aligned} C_0(x) &= (2x + 1)(x - 1)^2 \\ C_1(x) &= x(x - 1)^2 \\ C_2(x) &= x^2(3 - 2x) \\ C_3(x) &= x^2(x - 1) \\ dC_0/dx &= 2(x - 1)^2 + 2(x - 1)(2x + 1) \\ dC_1/dx &= (x - 1)^2 + 2x(x - 1) \\ dC_2/dx &= 2x(3 - 2x) - 2x^2 \\ dC_3/dx &= 2x(x - 1) + x^2, \end{aligned} \quad (6)$$

where x is a local coordinate defining a unit interpolation interval of $[0,1]$. Each of the basis functions has an associated node. Two of these nodes are data values (at $x = 0$ and $x = 1$) and two are derivatives of the data (at $x = 0$ and $x = 1$). Each cardinal function is a cubic polynomial with the property that its value is 1.0 for a particular node and 0.0 for all other nodes.

In three dimensions, 64 cardinal basis functions are formed from products of the one-dimensional functions:

$$\begin{aligned} \phi_{abc}(\alpha, \beta, \gamma) &= C_a(\alpha)C_b(\beta)C_c(\gamma) \\ a, b, c &= 0, \dots, 3, \end{aligned} \quad (7)$$

where α, β, γ are the local coordinates within the interpolating unit cube. There are 64 nodal values associated with the 64 basis functions: (η ; η_s ; η_r ; η_c ; η_{sr} ; η_{rc} ; η_{sc} ; η_{src}), where η represents the voxel value and its derivatives at each corner

of the unit cube. The derivatives were estimated numerically by central differencing. As in one dimension, each three-dimensional basis function has a value or derivative equal to 1.0 for a given node and 0.0 for all other nodes.

An interpolated value is calculated by summing the products of all 64 nodal values, η , and the associated basis functions, ϕ . The terms required for the Levenberg-Marquardt update then become

$$f_i(\mathbf{g}) = \sum_{a=0}^3 \sum_{b=0}^3 \sum_{c=0}^3 \eta_{abc} C_a(\alpha) C_b(\beta) C_c(\gamma) - A \quad (8)$$

$$J_{i,1}(\mathbf{g}) = \sum_{a=0}^3 \sum_{b=0}^3 \sum_{c=0}^3 \eta_{abc} \frac{\partial C_a(\alpha)}{\partial \alpha} C_b(\beta) C_c(\gamma)$$

$$J_{i,2}(\mathbf{g}) = \sum_{a=0}^3 \sum_{b=0}^3 \sum_{c=0}^3 \eta_{abc} C_a(\alpha) \frac{\partial C_b(\beta)}{\partial \beta} C_c(\gamma) \quad (9)$$

$$J_{i,3}(\mathbf{g}) = \sum_{a=0}^3 \sum_{b=0}^3 \sum_{c=0}^3 \eta_{abc} C_a(\alpha) C_b(\beta) \frac{\partial C_c(\gamma)}{\partial \gamma}.$$

This method of interpolation has several advantages from a computer-coding standpoint. The only function subroutines required are the four one-dimensional cardinal basis functions and their derivatives [eq (6)]. Terms required for the Levenberg-Marquardt update are simply repeated calls to the cardinal function subroutines, with multiplication by the appropriate nodal values and summation. Some care is required to maintain the proper association between nodal values and cardinal functions, but this can be handled with simple logic applied to the loop indices. The nodal values, η_{abc} , are not included in the partial derivatives of the Jacobian terms, since they are constant within each interpolation interval and are therefore independent of \mathbf{g} . This technique represents true interpolation in that voxel values are preserved.

Calculation of the Strain Tensor Field

The result of minimization of eq (1) for each location (\mathbf{p}) is the displacement vector field. The strain tensor field is calculated from these displacements. As a first step, the displacement field is smoothed using a local polynomial fit of a quadratic function to each component of the displacement vector. The strain field is then calculated from the smoothed displacement field by fitting a second-order approximation of the strain tensor to a local cloud of displacement values.³⁷ The number of data points that are included in the polynomial fit and strain calculation can be varied to control the degree of displacement filtering. The number of points is referred to as the span, which is denoted as k . Invariant quantities of interest are then calculated from the strain tensor.

An important aspect of the strain measurement calculation is the proper handling of points where the displacement measurement routine encountered difficulty. Nonlinear minimizations of the type required for displacement measurement are computationally difficult, particularly in this application where the material microarchitecture is used to construct the objective function. If there is insufficient local texture within the image data, then objective function minima will be poorly defined. If a poor starting point for the minimization

routine is determined, then convergence to a local minimum is possible.

Two behaviors are typically noted in these cases. Either convergence is slow when a region of the objective function is entered without a well-defined minimum, or convergence is to a region of parameter space outside of expected bounds. Both of these possibilities are identified during each displacement measurement by flagging points that fail to converge within a set number of iterations, or converge with a total displacement greater than a set value. Flagged points are simply eliminated from the strain calculation routine, and gradients are estimated from the remaining displacement values within the span setting.

All of the correlation and strain calculations were implemented in C code on a SPARCstation 10 (Sun Microsystems, Inc., Mountain View, California) with a single 166-MHz processor, 128Mb of RAM and a 9-Gb hard drive. A correlation job of approximately 5000 points requires between 9 and 10 h of CPU time, or about 6.5 to 7 s per point. Increasing the amount of RAM to slightly over 300 Mb, which would allow simultaneous core storage of both 150-Mb image volumes, would substantially reduce the computation time by eliminating hard disk swapping.

Characterization of Measurement Precision

Measurement characteristics of the three-dimensional texture correlation procedure were evaluated by correlation of repeat unloaded image data sets gathered for trabecular bone tissue from two different anatomic sites: a lumbar vertebral body (the spine in the lower back) and the proximal tibia (near the knee within the shin bone). Tissue from two different sites was chosen to evaluate stability of the technique with different sample microarchitectural characteristics.

Examination of the zero-strain condition was the most convenient way to develop an estimate of displacement and strain with these materials. Unlike two-dimensional speckle-based correlation that can be evaluated with simple materials, texture correlation by its very nature is most useful for materials with complex and inhomogeneous constitutive characteristics. This makes the local strain environment, even for test samples of simple geometry and under standard nominal loading conditions, very difficult to predict. It would be useful to confirm these precision estimates in strained samples where deformation of the subvolumes in the loaded data sets occurs, but this is at present impractical. Correlation of repeat unloaded data sets captures all of the sources of measurement error except for this relative distortion between the subvolumes as defined in the unloaded data set and the same region within a loaded sample. As with other correlation procedures, however, imprecision caused by this relative distortion (noise) increases in rough proportion with the amount of strain in the sample (signal). The zero-strain evaluation of measurement precision is therefore useful as an initial error characterization approach.

Cores of trabecular bone tissue were extracted from frozen cadaveric samples with a diamond-grit abrasive tool (nominal 5/8-in. diameter; 14.5-mm diameter extracted core). The cores were faced to a final length of 18 mm by machining each end with a 40-mm diameter conical abrasive cutter. Facing was accomplished while the cores were frozen in a custom liquid-nitrogen-supplied jig to limit damage to the trabecular architecture. Once machined, the cores were thawed and

acrylic platens were secured with a viscous cyanoacrylate adhesive. The sample/platen assemblies were placed within the loading jig, which was then mounted onto the scanner sample stage.

Each sample was imaged twice under the conditions described previously. Displacements were measured for approximately 5500 points distributed throughout the sample volume using a correlation subvolume size of $61 \times 61 \times 61$ voxels. Three different results were generated from the data. First, normality of the displacement error was evaluated by generating histograms of displacement magnitude for each sample. Second, the magnitude of the error was evaluated for each component of the displacement vector and strain tensor fields calculated throughout each sample. Third, the effect of varying the span used for filtering and strain calculation was evaluated by measuring the strain tensor field for k values between 40 and 100.

Example Application

Two additional samples were studied to both illustrate use of the technique and further assess measurement characteristics. Cores of trabecular bone from the distal femurs (the thigh bone near the knee) of two different cadavers were prepared in the standard way. The first sample was loaded to nominal strain values of 0.004 and 0.008, both levels being within the elastic range likely for this type of material. The second sample was loaded to nominal strains of 0.006 and 0.018, the first load level prior to sample yield and the second after localized collapse. Minimum principal strain was plotted within the sample interiors and compared with the local trabecular microarchitecture of the samples.

Results and Discussion

Renderings of the vertebral body and proximal tibia samples used for measurement precision characterization show the range of microarchitectures encountered in trabecular bone (Fig. 3).

Half of the image data for each sample were rendered to reveal internal microarchitectural details. The vertebral body sample is a lattice of rodlike components near the sample ends and an assembly of platelike components near the center. The proximal tibia sample is rodlike throughout, but the top and bottom halves exhibit different sizes and spacing of the structural components.

Characterization of Measurement Precision

Histograms of the displacement magnitude values measured by correlation of the repeat unloaded image volumes revealed normally distributed displacement errors (Fig. 4). This measurement characteristic is important to establish because the strain calculation assumes normally distributed displacement errors.³⁷ Since the distributions were normal, standard deviation was considered a suitable measure of precision. The standard deviations for the raw (unfiltered) displacement magnitudes were 0.036 voxels (1.26 μm) for the vertebral body sample and 0.038 voxels (1.34 μm) for the proximal tibia sample.

Consistent levels of precision were found for both samples after displacement filtering and strain calculation (Table 1).

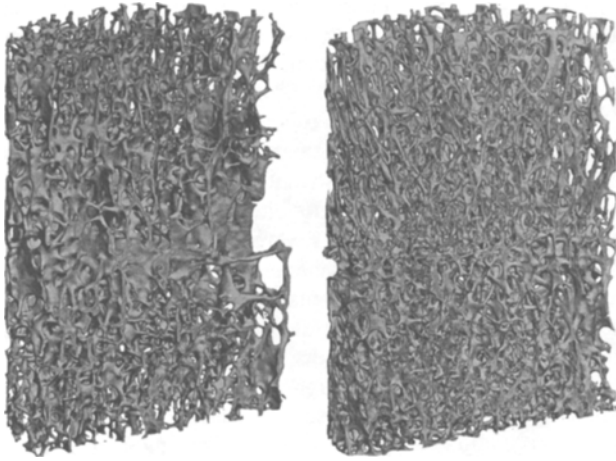


Fig. 3—Renderings derived from the microCT scans of the vertebral body (left) and proximal tibia (right) samples used for assessment of measurement precision

Standard deviations for components of the displacement vector averaged 0.035 voxels ($1.23 \mu\text{m}$) for both samples, with a range of 0.030 voxels ($1.05 \mu\text{m}$) to 0.044 voxels ($1.54 \mu\text{m}$). Strain tensor components varied by an average of 302 μstrain for the vertebral body sample, with a range of 211 to 401, and by 289 μstrain for the proximal tibia sample, with a range of 211 to 457. The shear strain components were consistently more precise than the normal strain components. Variation in strain precision as a function of the span (k value) used for filtering and strain calculation showed the expected trend (Fig. 5). Averages for the standard deviations of all strain components dropped from 348 μstrain for a 40-point (2.47 mm) span to 223 μstrain for a 100-point (3.45 mm) span. One advantage of working in three dimensions is that the diameter of a typical local region used for strain calculation increases slowly with the number of points in the region. Measurement error can be reduced by increasing the span, therefore, without large decreases in spatial resolution.

The values for displacement and strain precision are similar to equivalent values for two-dimensional digital image correlation, which are typically in the range of 0.02 pixels for displacements and 0.0002 (200 μstrain) for strains.⁷ The differences are likely due to the greater levels of noise in the three-dimensional data sets compared with simple planar images. The tomographic reconstructions used here were generated from 400 planar images, each an image intensifier amplification of an X-ray projection. Three-dimensional reconstruction embodies both signal and noise from all of these images. Since correlation is sensitive to noise, it is not surprising that error levels are greater. The fact that they are of similar magnitudes, however, indicates that overall the characteristics of the measurement techniques are similar.

Measurement precision must also be considered in the context of total amount of signal within typical samples. For trabecular bone, the very earliest evidence of yielding begins at nominal strains of approximately 0.006 (6000 μstrain), and macroscopic local failure does not begin until the 0.01 (10,000 μstrain) level.³⁸ Measurement uncertainty, therefore,

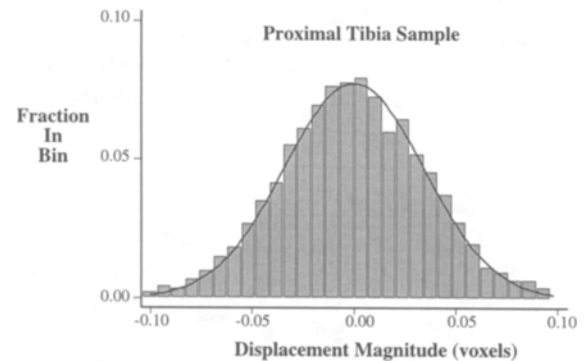
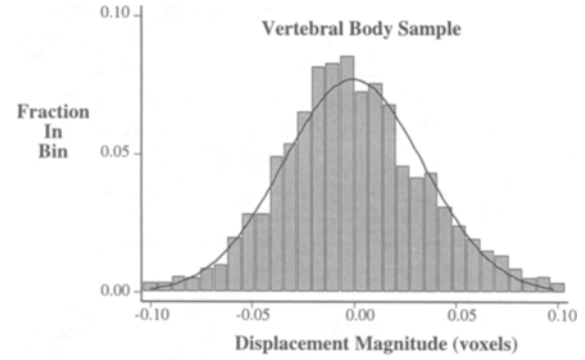


Fig. 4—Histograms of displacement magnitude for correlation of the repeat unloaded data sets

TABLE 1—STANDARD DEVIATION VALUES FOR DISPLACEMENTS (d) AND STRAINS (ϵ) (MEASURED FROM THE REPEAT UNLOADED IMAGE DATA VOLUMES)^a

	Vertebral Body Sample	Proximal Tibia Sample
d_s (voxels)	0.031	0.030
d_r (voxels)	0.040	0.044
d_c (voxels)	0.036	0.031
d (average)	0.035	0.035
ϵ_{ss} (μ strain)	370	280
ϵ_{rr} (μ strain)	401	323
ϵ_{cc} (μ strain)	366	457
ϵ_{sr} (μ strain)	211	239
ϵ_{rc} (μ strain)	247	211
ϵ_{sc} (μ strain)	217	224
ϵ (average)	302	289

NOTE: Components are given in the s, r, c (slice, row, column) imaging coordinate system. Voxels are in 35- μm cubes. Strain calculation was performed with a span (k value) of 60. Standard deviations are consistent between the two sample types and are similar to values for two-dimensional image correlation

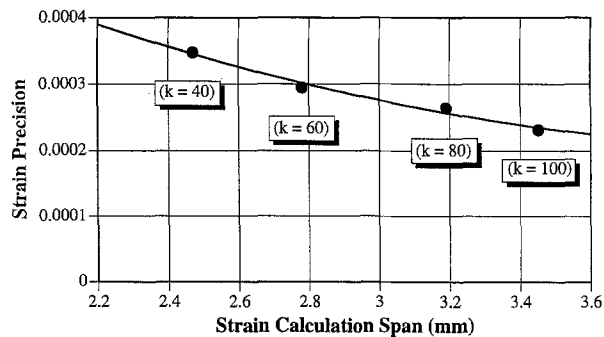


Fig. 5—Strain precision as a function of strain calculation range

is approximately 5 percent of the nominal strain for a sample loaded to the upper end of the elastic region. This is adequate for reliable mapping of elastic strain patterns.

Example Application

Two femoral condyle samples were examined at different nominal strain levels to evaluate the consistency of strain measurement within the elastic range and the ability to track patterns of strain development into the postyield region. The first femoral condyle sample was evaluated at two different elastic range nominal strains: 0.004 (4000 μ strain) and 0.008 (8000 μ strain). Minimum principal strain contours plotted within the sample (Fig. 6) show virtually identical spatial patterns when each plot is autoscaled to its own maximum value, as expected for linear elastic material behavior. When both plots are scaled to the maximum value of the more highly strained sample, the development of the strain pattern is revealed. Strain concentrates within the less dense lower portion of the sample, with a discrete boundary formed by a dense plane of material perpendicular to the longitudinal axis in the center of the sample. Deformation of the sample is shown on an exaggerated scale to render visible overall shape changes.

The second femoral condyle sample was examined at nominal strains of 0.006 (6000 μ strain) and 0.018 (18,000 μ strain). The first level is within the elastic range; the second is beyond the initial stages of yield. Minimum principal strain develops to the highest degree within the lower portion of the sample (Fig. 7), and very high local strains appear after sample failure. Plots are shown with both linear and logarithmic scales to reveal details across the broad range of strains. In this sample, the dense plane of material is oriented obliquely to the longitudinal axis of the sample. The two patterns are consistent with each other and follow the oblique orientation of the dense plane, with the highest strains and localized failure occurring on the bottom portion of the sample where material density appears to be lower.

For both femoral condyle samples, the local strains reached levels several times greater than the nominal strain level, even for elastic loading levels. This has implications for the development of elastoplastic constitutive relationships. If these are developed based on results of nominal measurements made from standard material test samples, then local material behavior will not be accurately represented. Yield-

ing will be predicted on a local level much sooner than it actually occurs. The relationship between local material architecture and the ability to achieve high elastic strains is not well understood but is an important factor in modeling failure and postyield behavior.

Local continuum-level strains reaching levels of 6 to 7 percent, yet still exhibiting linear elastic behavior, highlights the limitations of standard continuum approaches to the modeling of material behavior in foam materials. Small regions of the foam truss can be deformed to substantial degrees by inducing bending within individual struts, producing steep local displacement gradients. These steep displacement gradients appear as high local strains at the continuum level. Micropolar formulations, or models that represent material architecture directly, may be required to capture these effects. Improving the digital volume correlation technique, through the addition of rotation and strain parameters, will also allow these localized effects to be measured more accurately.

Limitations and Future Work

Several limitations of this study must be acknowledged. The sum-of-squares formulation is computationally efficient but is also susceptible to differences in background intensities between the unloaded and loaded image volumes. Although this appears to be less of a problem with image data generated by tomography, it should be evaluated directly by analysis with more traditional cross-correlation functions. We have also implemented a simple displacement-only formulation for this initial study, again for reasons of computational efficiency. Future work will involve an expanded formulation, with both rotational and strain parameters. This will be conducted in conjunction with the collection of experimental data for rigid body translations and rotations of samples within the scanning system. A more complete evaluation of measurement precision and reliability will emerge from these studies.

Conclusions

Methods of digital image correlation have been modified and extended into three dimensions for certain classes of materials. The full continuum-level three-dimensional strain tensor field is mapped throughout the interior of samples. Appropriate materials are those with microarchitectures that can be resolved by high-resolution tomography methods. Initial characterization of the method for trabecular bone samples (a naturally occurring rigid foam) imaged by cone beam X-ray tomography at a resolution of 35 μ m revealed a displacement measurement precision of 0.035 voxels (1.23 μ m) and a strain measurement precision of approximately 0.0003 (300 μ strain). This level of precision is adequate for measurement of elastic range strain patterns within trabecular bone, where macroscopic localized failure typically begins at nominal strains of 0.01 (10,000 μ strain). The technique is also robust past sample yield, when local strain magnitudes can approach 0.15 (150,000 μ strain).

Acknowledgments

This research was supported by a grant from the National Institutes of Health (NIH R01 AR43183).

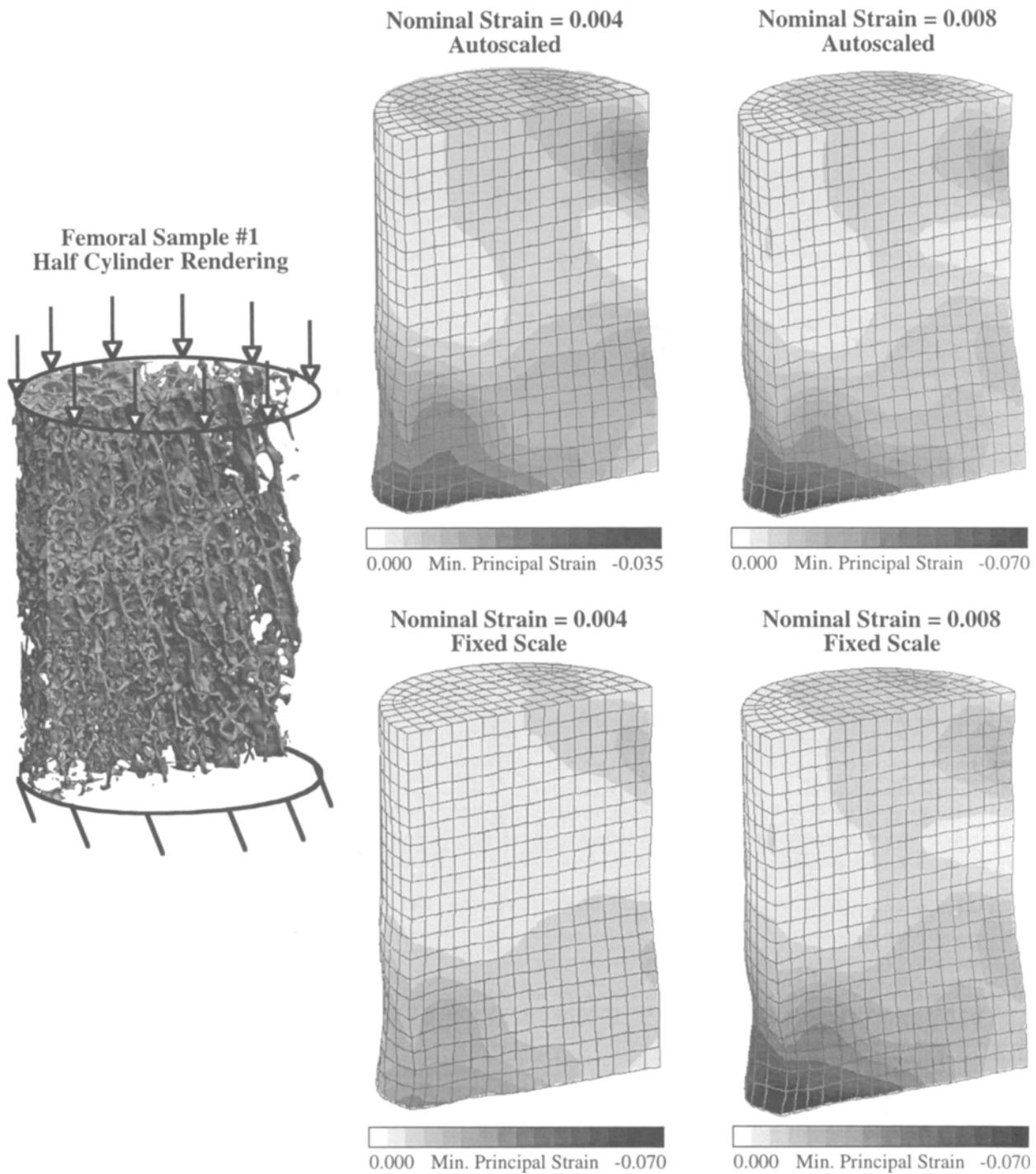


Fig. 6—Minimum principal strains measured within the first femoral condyle sample, loaded in axial compression to two elastic range nominal strains

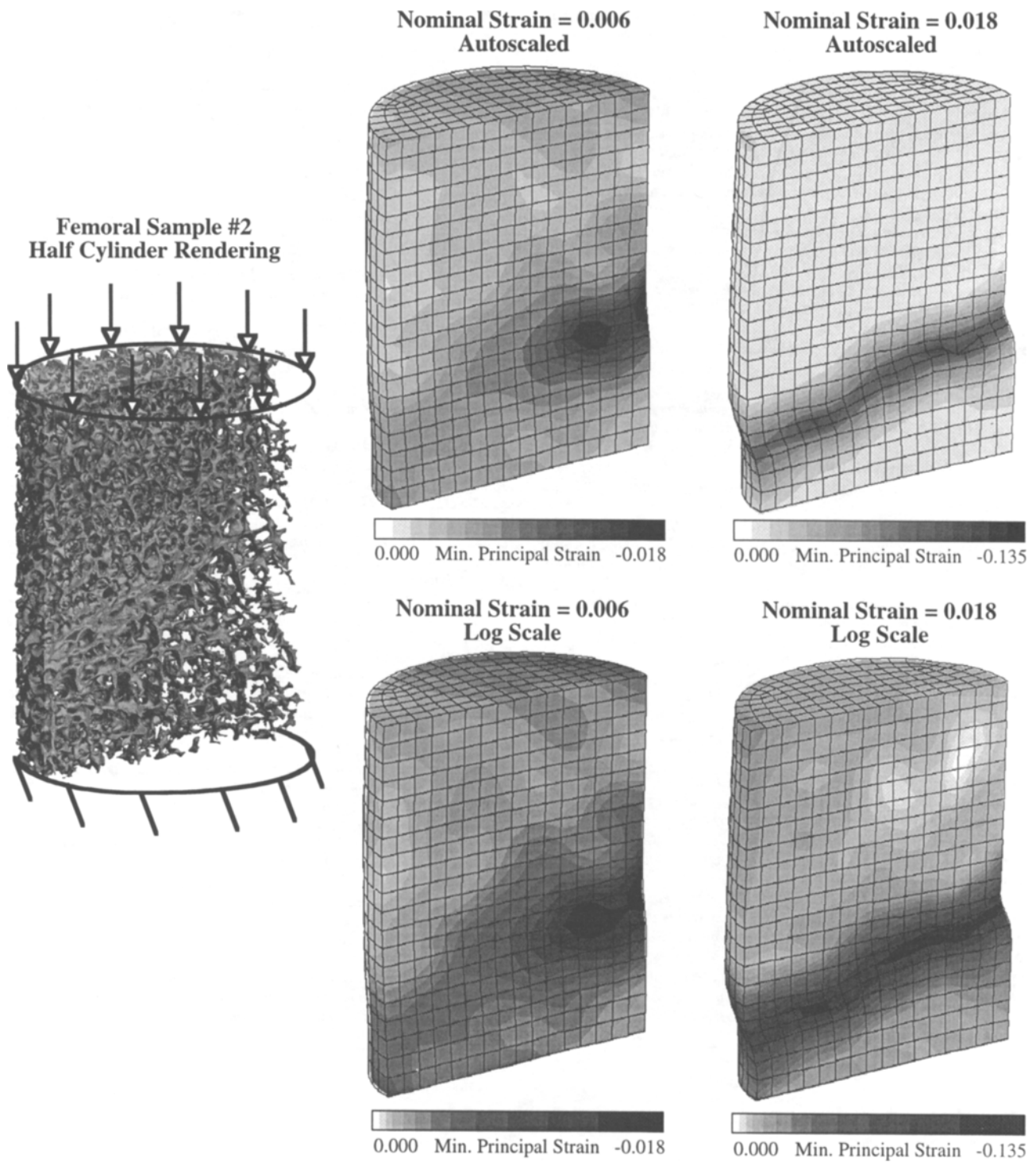


Fig. 7— Minimum principal strains measured within the second femoral condyle sample, loaded in axial compression to elastic (0.006) and plastic (0.018) range nominal strains

References

1. Bruck, H.A., McNeill, S.R., Sutton, M.A., and Peters, W.H., III, "Digital Image Correlation Using Newton-Raphson Method of Partial Differential Correction," *EXPERIMENTAL MECHANICS*, **29**, 261-267 (1989).
2. Chu, T.C., Ranson, W.F., Sutton, M.A., and Peters, W.H., "Applications of Digital-image-correlation Techniques to Experimental Mechanics," *EXPERIMENTAL MECHANICS*, **25**, 232-244 (1985).
3. Kahn-Jetter, Z.L., Jha, N.K., and Bhatia, H., "Optimal Image Correlation in Experimental Mechanics," *Opt. Eng.*, **33**, 1099-1105 (1994).
4. Sutton, M.A., Wolters, W.J., Peters, W.H., Ranson, W.F., and McNeill, S.R., "Determination of Displacements Using an Improved Digital Correlation Method," *Image Vis. Computing*, **1**, 133-139 (1983).
5. Sutton, M.A., Cheng, M., Peters, W.H., Chao, Y.J., and McNeill, S.R., "Application of an Optimized Digital Correlation Method to Planar Deformation Analysis," *Image Vis. Computing*, **4**, 143-150 (1986).
6. Boegli, V. and Kern, D.P., "Automatic Mark Detection in Electron Beam Nanolithography Using Digital Image Processing and Correlation," *J. Vacuum Sci. Tech.*, **8**, 1994-2001 (1990).
7. Lyons, J.S., Liu, J., and Sutton, M.A., "High-temperature Deformation Measurements Using Digital-image Correlation," *EXPERIMENTAL MECHANICS*, **36**, 64-70 (1996).
8. McNeill, S.R., Peters, W.H., and Sutton, M.A., "Estimation of Stress Intensity Factor by Digital Image Correlation," *Eng. Fract. Mech.*, **28**, 101-112 (1987).
9. Manduchi, R. and Mian, G.A., "Accuracy Analysis for Correlation-based Image Registration Algorithms," *IEEE International Symposium on Circuits and Systems*, Chicago (1993).
10. Sutton, M.A., McNeill, S.R., Jang, J., and Babai, M., "Effects of Sub-pixel Image Restoration on Digital Correlation Error Estimates," *Opt. Eng.*, **27**, 870-877 (1988).
11. Tolat, A.R., McNeill, S.R., and Sutton, M.A., "Effects of Contrast and Brightness on Subpixel Image Correlation," *Proceedings of the Twenty-Third Southeastern Symposium on System Theory*, Columbia, South Carolina (1991).
12. Russell, S.S. and Sutton, M.A., "Strain-field Analysis Acquired Through Correlation of X-ray Radiographs of a Fiber-reinforced Composite Laminate," *EXPERIMENTAL MECHANICS*, **29**, 237-240 (1989).
13. Bay, B.K., "Texture Correlation: A Method for the Measurement of Detailed Strain Distributions Within Trabecular Bone," *J. Orthopaedic Res.*, **13**, 258-267 (1995).
14. Helm, J.D., McNeill, S.R., and Sutton, M.A., "Improved Three-dimensional Image Correlation for Surface Displacement Measurement," *Opt. Eng.*, **35**, 1911-1920 (1996).
15. Kahn-Jetter, Z.L. and Chu, T.C., "Three-dimensional Displacement Measurements Using Digital Image Correlation and Photogrammetric Analysis," *EXPERIMENTAL MECHANICS*, **30**, 10-16 (1990).
16. Durand, E.P. and Rueggeger, P., "Cancellous Bone Structure: Analysis of High-resolution Ct Images with the Run-length Method," *J. Computer Assisted Tomography*, **15**, 133-139 (1991).
17. Elke, R.P.E., Cheal, E.J., Simmons, C., and Poss, R., "Three-dimensional Anatomy of the Cancellous Structures Within the Proximal Femur from Computed Tomography Data," *J. Orthopaedic Res.*, **13**, 513-523 (1995).
18. Feldkamp, L.A., Goldstein, S.A., Parfitt, A.M., Jesion, G., and Kleerekoper, M., "The Direct Examination of Three-dimensional Bone Architecture In Vitro by Computed Tomography," *J. Bone Mineral Res.*, **4**, 3-11 (1989).
19. Flynn, M.J. and Cody, D.D., "The Assessment of Vertebral Bone Macroarchitecture with X-ray Computed Tomography," *Calcified Tissue Int.*, **53**, S170-S175 (1993).
20. Kuhn, J.L., Goldstein, S.A., Feldkamp, L.A., Goulet, R.W., and Jesion, G., "Evaluation of a Microcomputed Tomography System to Study Trabecular Bone Structure," *J. Orthopaedic Res.*, **8**, 833-842 (1990).
21. Bart-Smith, H., Bastawros, A.F., Mumm, D.R., Evans, A.G., Sypek, D.J., and Wadley, H.N.G., "Compressive Deformation and Yielding Mechanisms in Cellular Al Alloys Determined Using X-ray Tomography and Surface Strain Mapping," *Acta Materialia*, **46**, 3583-3592 (1998).
22. Breunig, T.M., Stock, S.R., and Brown, R.C., "Simple Load Frame for In Situ Computed Tomography and X-ray Tomographic Microscopy," *Mat. Eval.*, **51**, 596-600 (1993).
23. Burch, S.F. and Lawrence, P.F., "Recent Advances in Computerized X-ray Tomography Using Real-time Radiography Equipment," *Brit. J. NDT*, **34**, 129-133 (1992).
24. Deis, T.A. and Lannutti, J.J., "X-ray Computed Tomography for Evaluation of Density Gradient Formation During the Compaction of Spray-dried Granules," *J. Am. Ceramic Soc.*, **81**, 1237-1247 (1998).
25. Drake, S.G., "Improved Real-time X-ray Technology Widens the Horizons of Industrial Computer Tomography," *Brit. J. NDT*, **35**, 580-583 (1993).
26. Jasti, J.K., Jesion, G., and Feldkamp, L., "Microscopic Imaging of Porous Media with X-ray Computer Tomography," *SPE Formation Eval.*, **8**, 189-193 (1993).
27. Kropas, C.V., Moran, T.J., and Yancey, R.N., "Effect of Composition on Density Measurement by X-ray Computed Tomography," *Mat. Eval.*, **49**, 487-490 (1991).
28. Lambrineas, P., Davis, J.R., Suendermann, B., Wells, P., Thomson, K.R., Woodward, R.L., Egglestone, G.T., and Challis, K., "X-ray Computed Tomography Examination of Inshore Mine-hunter Hull Composite Material," *NDT&E Int.*, **24**, 207-213 (1991).
29. Lavebratt, H., Ostman, E., Persson, S., and Stenberg, B., "Application of Computed X-ray Tomography Scanning in the Study of Thermo-oxidative Degradation of Thick-walled Filled Natural Rubber Vulcanizates," *J. Appl. Polymer Sci.*, **44**, 83-94 (1992).
30. London, B., Yancey, R.N., and Smith, J.A., "High-resolution X-ray Computed Tomography of Composite Materials," *Mat. Eval.*, **48**, 604-608 (1990).
31. Phillips, D.H. and Lannutti, J.J., "Measuring Physical Density with X-ray Computed Tomography," *NDT&E Int.*, **30**, 339-350 (1997).
32. Watson, A.T. and Mudra, J., "Characterization of Devonian Shales with X-ray Computed Tomography," *SPE Formation Eval.*, **9**, 209-212 (1994).
33. Reimann, D.A., Hames, S.M., Flynn, M.J., and Fyhrie, D.P., "A Cone Beam Computed Tomography System for True 3D Imaging of Specimens," *Appl. Radiation Isotopes*, **48** (10-12), 1433-1436 (1997).
34. Feldkamp, L.A., Davis, L.C., and Kress, J.W., "Practical Cone-beam Algorithm," *J. Opt. Soc. Am. A*, **1**, 612-619 (1984).
35. Gill, P.E., Murray, W., and Wright, M.H., *Practical Optimization*, Academic Press, London, 133-140 (1981).
36. Lancaster, P. and Salkauskas, K., *Curve and Surface Fitting—An Introduction*, Academic Press, London, 190 (1986).
37. Geers, M.G.D., De Borst, R., and Brekelmans, W.A.M., "Computing Strain Fields from Discrete Displacement Fields in 2D-solids," *Int. J. Solids Struct.*, **33**, 4293-4307 (1996).
38. Keaveny, T.M., Guo, X.E., Wachtel, E.F., McMahon, T.A., and Hayes, W.C., "Trabecular Bone Exhibits Fully Linear Elastic Behavior and Yields at Low Strain," *J. Biomechanics*, **27**, 1127-1136 (1994).